

A quantum phase transition from triangular to stripe charge order in NbSe₂

Anjan Soumyanarayanan,^{1,2,*} Michael M. Yee,¹ Yang He,¹ Jasper van Wezel,^{3,4} D.J. Rahn,⁵ K. Rossnagel,⁵ E.W. Hudson,⁶ M.R. Norman,³ and Jennifer E. Hoffman^{1,†}

¹*Department of Physics, Harvard University, Cambridge, MA 02138, USA*

²*Department of Physics, Massachusetts Institute of Technology, Cambridge, MA 02139, USA*

³*Materials Science Division, Argonne National Laboratory, Argonne, IL 60439, USA*

⁴*H. H. Wills Physics Laboratory, University of Bristol, Bristol BS8 1TL, UK*

⁵*Institute of Experimental and Applied Physics, University of Kiel, 24098 Kiel, Germany*

⁶*Department of Physics, Pennsylvania State University, State College, PA 02138, USA*

The competition between proximate electronic phases produces a complex phenomenology in strongly correlated systems. In particular, fluctuations associated with periodic charge or spin modulations, known as density waves, may lead to exotic superconductivity in several correlated materials. However, density waves have been difficult to isolate in the presence of chemical disorder, and the suspected causal link between competing density wave orders and high temperature superconductivity is not understood. Here we use scanning tunneling microscopy to image a previously unknown unidirectional (stripe) charge density wave (CDW) smoothly interfacing with the familiar tri-directional (triangular) CDW on the surface of the stoichiometric superconductor NbSe₂. Our low temperature measurements rule out thermal fluctuations, and point to local strain as the tuning parameter for this quantum phase transition. We use this discovery to resolve two longstanding debates about the anomalous spectroscopic gap and the role of Fermi surface nesting in the CDW phase of NbSe₂. Our results highlight the importance of local strain in governing phase transitions and competing phenomena, and suggest a new direction of inquiry for resolving similarly longstanding debates in cuprate superconductors and other strongly correlated materials.

A. INTRODUCTION

While a classical phase transition separates two states of matter at different temperatures, two ordered ground states of a material at zero temperature are separated by a quantum critical point (QCP). The competition between proximate ordered phases near the QCP can dramatically influence a large region of the phase diagram[1]. While the fluctuations from competing quantum states lead to exotic physics even at higher temperatures, low temperature studies of these states can lead to a better understanding of the root of the competition. Density waves - charge or spin ordered states of collective origin driven by instabilities of the Fermi surface (FS) - exist in close proximity to superconductivity (SC) in several classes of correlated materials[2–4], and various proposals have recently emerged to study their interplay in the presence of strong inhomogeneity in these systems[5]. In this light, it is surprising that charge density waves (CDWs) are not fully understood even in the weakly correlated and stoichiometric transition metal dichalcogenides (TMDCs). While a classic CDW arises from strong FS nesting, resulting in a sharply peaked susceptibility and a Kohn anomaly at

the CDW wavevector, the quasi-2D TMDCs are known to deviate from this picture[6].

2H-NbSe₂ is a layered TMDC which has generated much recent interest[7–9] as a model system for understanding the interplay of the CDW and SC phases which onset at $T_{\text{CDW}} \sim 33$ K and $T_{\text{SC}} \simeq 7.2$ K respectively[10, 11]. Despite extensive study[8, 12–15], several key facts about its familiar tri-directional ($3Q$) CDW remain unresolved, including the role of FS nesting in determining its wavevector \vec{q}_{3Q} , and the magnitude of the spectral gap and its role in the energetics of the transition. First, angle-resolved photoemission (ARPES) studies have been unable to uniquely identify \vec{q}_{3Q} -nested FS regions in *2H*-NbSe₂[8, 12, 15–19]. Meanwhile, recent studies indicate a broadly peaked susceptibility and a soft phonon over a range of wavevectors around \vec{q}_{3Q} [6, 14, 15], suggesting instead that the q -dependence of the electron-phonon coupling could play an important role in driving the transition. Second, kinks in tunneling spectra at ± 35 mV ($\pm \varepsilon_K$), historically identified as gap edges, correspond to an anomalously large energy scale for the corresponding T_{CDW} ($2\varepsilon_K/3.5k_B T_{\text{CDW}} \sim 7.05$)[20], while recent ARPES studies indicate a much smaller $\sim 3 - 5$ mV gap[12, 15].

Our discovery, by low-temperature scanning tunneling microscopy (STM), of a $1Q$ CDW with distinct wavelength and tunneling spectra from the $3Q$ CDW, in conjunction with band structure calculations, allows us to resolve both longstanding questions of the wavevector and the gap. First, the distinct wavelengths demonstrate that FS nesting plays a negligible role in setting their magnitude. Second, the distinct tunneling spectra of the $1Q$ CDW region help us disentangle the $3Q$ CDW spectra to expose a particle-hole asymmetric gap, riding on top of a strong inelastic background.

B. RESULTS

Fig. 1A shows a topographic image of a locally commensurate ($3a_0$) CDW. Its microscopic $3Q$ nature is confirmed by the existence of a secondary CDW peak in the Fourier Transform (FT) in Fig. 1B, in contrast to bulk measurements[9]. Phase slips result in an overall periodicity of $\lambda_{3Q} \simeq 3.05 a_0$, corresponding to $\vec{q}_{3Q} \simeq 0.328 \vec{Q}_0$, where \vec{Q}_0 is the Bragg vector[9, 10, 21]. Our primary experimental discovery is shown in Fig. 2A, where regions of unidirectional ($1Q$) CDW with unique wavevector \vec{q}_{1Q} along a single $3Q$ direction form an atomically smooth interface with the $3Q$ CDW. The absence of atomic lattice discontinuities rules out the possibility of a NbSe₂ polytype interface[22]. While other TMDCs are known to exhibit a thermally induced triclinic CDW state that varies with doping near T_{CDW} [21, 23], no such anisotropy has been reported in $2H$ -NbSe₂. Moreover, our observations are at temperatures $T \ll T_{\text{CDW}}$, where thermal fluctuations are insignificant, implying that the $1Q$ CDW is a distinct quantum phase.

The $1Q$ CDW regions take the form of elevated topographic ribbons, exemplified in Fig. 2B-C, suggesting a strain-induced phase (§ SI II). The observation of Y -junctions between ribbons with differently oriented \vec{q}_{1Q} rules out extrinsic uniaxial strain and suggests instead locally varying strain, perhaps due to underlying defects causing nanoscale buckling of the top few atomic layers. From a survey of several ribbons, we place upper bounds of 3% on the vertical strain and 0.06% on the lateral strain (see § SI II).

Fig. 3A-B show the dominant Fourier peak for the $1Q$ modulation, $\vec{q}_{1Q} \simeq 2/7 \vec{Q}_0$, corresponding to a wavelength, $\lambda_{1Q} \simeq 3.5 a_0$. No similar periodicity or rich harmonic structure has thus far been reported in any TMDC system[11]. We develop a phenomenological understanding of the $1Q$ harmonic structure following

McMillan's Landau theory[21, 24]. Rather than a uniform $3.5 a_0$ charge modulation, the system could lower its energy by locking the charge modulation to the lattice with $3 a_0$ periodicity. This would require compensation by a one atom phase slip every two oscillations, corresponding to a $2\pi/3$ discommensuration, as shown in Fig. 3C[21]. The resulting harmonic structure shown in Fig. 3D reproduces all observed peak positions. Moreover, the rich harmonic content we observe is another indication of the strong coupling of the electronic modulation to the lattice. An even better agreement with relative peak heights could be obtained by considering spatial variations in the order parameter amplitude[21].

The stark contrast between our observation of two CDW wavevectors \vec{q}_{1Q} and \vec{q}_{3Q} of same orientation but 13% difference in magnitude, and the recent X-ray measurements reported by Feng *et al.*[9], provides strong evidence against FS nesting at one particular wavevector as a driving force for either CDW. While our 13% wavevector difference arose from moderate anisotropic strain (up to 0.06% in-plane), Feng *et al.* applied hydrostatic pressure sufficient to induce in-plane lattice distortions up to 1.6%, yet observed no measurable deviation of the CDW wavevector from \vec{q}_{3Q} [9]. The observed insensitivity of q_{3Q} to hydrostatic pressure would clearly indicate that the FS does not qualitatively change in the presence of even relatively large lattice distortions, and would thus rule out a change in the FS as the source of our observed 13% wavevector difference. Furthermore, consistent with our experiment and with previous calculations[6, 14, 15], we find no sharp peak in the susceptibility (Fig. 4) computed from our modeled band structure (§ SI III). Therefore, our observations and calculations both indicate that the FS can play only a minor role in determining CDW wavevectors in NbSe₂. This highlights the key role that the q -dependence of alternative mechanisms such as electron-phonon coupling may play in driving the transition, and particularly the manner in which these mechanisms may be influenced by local strain.

The two CDW regions display quite different tunneling spectra, as shown in Fig. 5A-B. We employ a fit to the NbSe₂ band structure (§ SI III), and impose a CDW wavevector \tilde{q} , gap $\tilde{\Delta}$, and broadening parameter $\tilde{\Gamma}$, to calculate the density of states (DOS), in Fig. 5C (§ SI IV). For the $3Q$ CDW state the measured dI/dV spectrum, proportional to the DOS, is best reproduced using $\tilde{q} = (0.333 \pm 0.004) Q_0$ (the observed local CDW periodicity), $\tilde{\Delta} = (12 \pm 2) \text{ mV}$ (which has not been previously apparent from direct observations by spectroscopic techniques), and $\tilde{\Gamma} = 5 \text{ mV}$. The calculations cap-

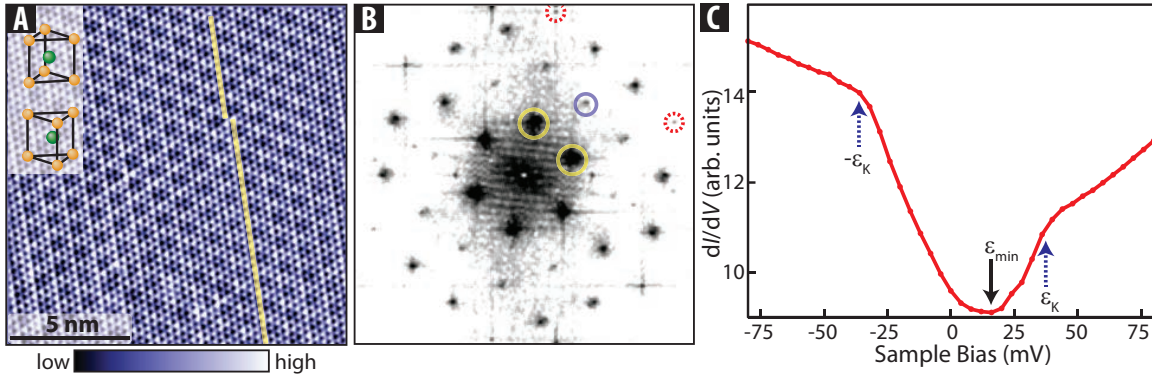


Figure 1: **STM of the 3Q CDW.** (A) Atomic resolution topograph showing the $\sim 3 a_0$ periodic CDW. Yellow lines are overlaid on a one atom shift of the CDW maximum (phase slip). Inset shows the crystal structure of $2H\text{-NbSe}_2$, with alternating layers of Nb (green) and Se (orange) atoms. (B) Fourier Transform (FT) of a larger (~ 45 nm) topograph, displaying a 3Q CDW. Primary CDW wavevectors, \vec{q}_1 and \vec{q}_2 (yellow circles), a secondary CDW wavevector, $\vec{q}_1 + \vec{q}_2$ (blue circle) and Bragg vectors (dashed red circles) are indicated. (C) Average dI/dV spectrum acquired from the area in A, showing kinks at $\sim \pm 35$ mV (ε_K), the minimum ε_{\min} offset from ε_F ($V_{\text{bias}} = 0$) by ~ 17 mV, and marked asymmetry about ε_F . Setpoint parameters: sample bias, $V_{\text{sample}} = -50$ mV (A), -60 mV (B), -80 mV (C); junction resistance, $R_J = 2.5$ G Ω (A), 0.1 G Ω (B), 0.4 G Ω (C); and RMS lock-in excitation, $V_{\text{mod}} = 3.5$ mV (C).

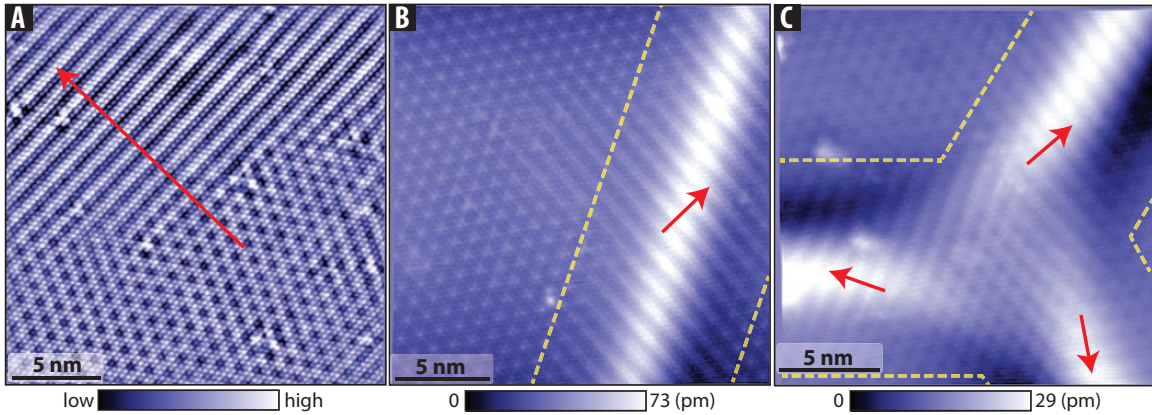


Figure 2: **The 1Q - 3Q Interface.** (A) Topograph showing an atomically smooth interface between the 3Q (bottom) and 1Q (top) CDWs. (B) Topograph showing formation of 1Q CDW along a 'ribbon'. Ribbons are typically 10 - 20 nm in width, and elevated by 20 - 40 pm. Dashed yellow lines indicate the approximate extent of the ribbon; the red arrow points along the 1Q CDW direction (\vec{q}_{1Q}). (C) Topograph showing a Y-junction between three such 1Q ribbons, each with a different 1Q CDW direction. The topograph in A has been leveled by removing a polynomial background to clearly show the CDW interface. Setpoint parameters: $V_{\text{sample}} = -50$ mV; $R_J = 1$ G Ω (A,C), 5 G Ω (B).

ture the overall shape, width, and center ε_{\min} of the gap structure within 30 mV of ε_F (§ SI IV). The fact that ε_{\min} is offset from ε_F should be unsurprising for a quasi-2D system[25], but had not been understood or observed in NbSe_2 until now, due to limitations of spectroscopic techniques which are sensitive to filled states only[12].

We disentangle the CDW gap from other effects in the 3Q spectra through a comparison with the 1Q spectra in Fig. 5B. These V-shaped 1Q spectra resemble the linear tunneling conductance background historically attributed to the inelastic coupling of tunneling electrons to a flat bosonic spectrum[26]. That this background

is much stronger in the 1Q region, obscuring band structure effects, is likely a strain-induced phenomenon, which may be related to the buckling and associated decoupling of the topmost layers in the 1Q region. Meanwhile, present in both 1Q and 3Q spectra (thus unlikely to be associated with these different CDWs), yet absent in calculations (thus unlikely to be a band structure effect), are the ± 35 mV kinks, previously and mistakenly identified as the CDW gap[20]. We universally observe the kinks even well above T_{CDW} , which further demonstrates their lack of bearing on the CDW phase (§ SI IV). ARPES studies observe a prominent band structure kink

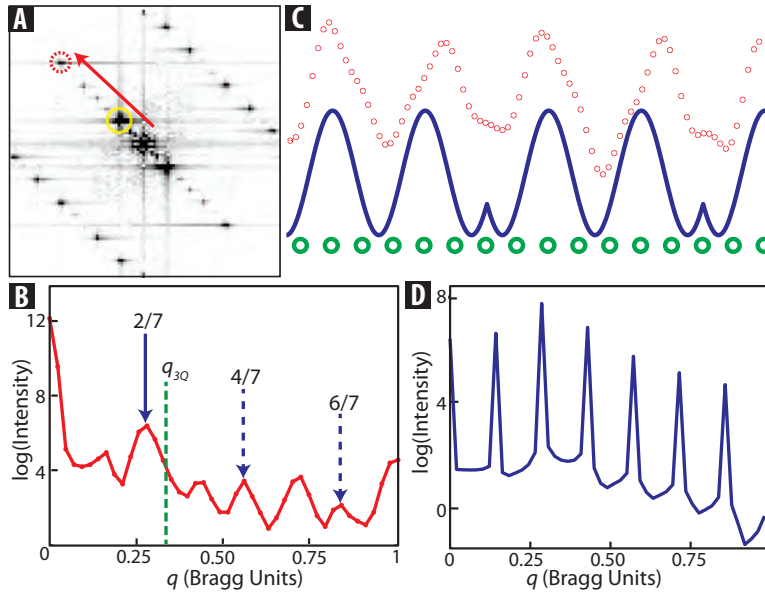


Figure 3: **The 1Q CDW.** (A) FT of the out-of-feedback current at +50 mV over a 1Q region (upper left quadrant of Fig. 2A). The dominant CDW wavevector (yellow circle) and Bragg vector (dashed red circle) are indicated. (B) Linecut of the FT intensity parallel to the red line in A from the center to the Bragg peak, in units of the Bragg vector \vec{Q}_0 . The dominant peak, $q_{1Q} \simeq 2/7Q_0$ (solid blue arrow) and its harmonics (dashed blue arrows) are identified, and are distinct from the $3Q$ wavevector q_{3Q} (dashed green line). The remaining peaks are Bragg reflections of these three peaks. Setpoint parameters: $V_{\text{sample}} = -50$ mV; $R_J = 0.2$ G Ω . (C) Phenomenological model of the observed 1Q wavelength, $\lambda_{1Q} \simeq 3.5 a_0$ (details in text). The atomic periodicity is indicated by green circles and the phase of the CDW order parameter from the model is shown in blue[21]. A topographic linecut (red dots) is extracted from Fig. 2A along the red arrow (\vec{q}_{1Q}), filtered to remove atomic corrugations, and overlaid for comparison. (D) Simulated FT intensity from the cartoon CDW modulation in C, for comparison with experimental peak positions in B.

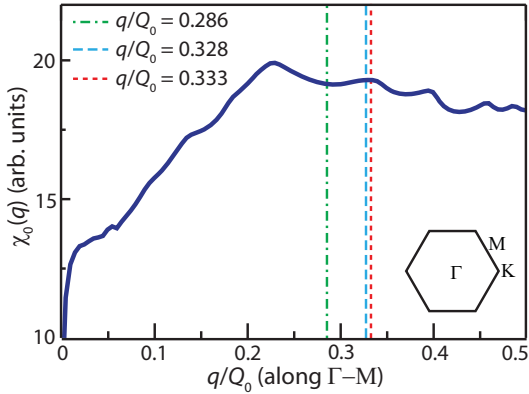


Figure 4: **Susceptibility.** The non-interacting susceptibility $\chi_0(q, \omega = 0)$ calculated from a fit to the $2H$ -NbSe₂ band structure (§ SI III) along the $\Gamma - M$ direction of the reciprocal lattice, displaying a broad maximum over a range of wavevectors: $\vec{q} \sim 0.25 - 0.4$ [6, 14, 15]. The CDW wavevectors q_{1Q} , q_{3Q} and $Q_0/3$ are overlaid for comparison. Inset shows the Brillouin Zone (BZ) of the hexagonal $2H$ -NbSe₂ lattice.

at a similar energy in the Se Γ -pocket[15, 18], attributed to coupling to an optical phonon[13]. We therefore conclude that this self-energy effect is responsible for the ε_K kinks in the tunneling spectra as well. The discrepancy

between the data and band structure calculations above ~ 30 mV in Fig. 5C can thus be attributed to the inelastic tunneling background and self-energy effects.

C. DISCUSSIONS

We therefore resolve a longstanding debate about the anomalous CDW gap magnitude reported by STM measurements[20], and caution that not all ε_F -symmetric kinks in tunneling spectra are associated with order (e.g. density wave or superconducting gaps). On the contrary, we emphasize that the true CDW signature in NbSe₂ is offset from ε_F , which has confused an active research community for two decades, and has been disentangled now only by a combination of spatially resolved filled and empty state spectroscopy of a proximate (1Q) phase, and band structure calculations[25]. This emphasizes the need for full experimental exploration of proximate phases in other pertinent materials, combined with quantitative modeling. We further suggest that controlled local strain, through epitaxy or intentional defects, may be a use-

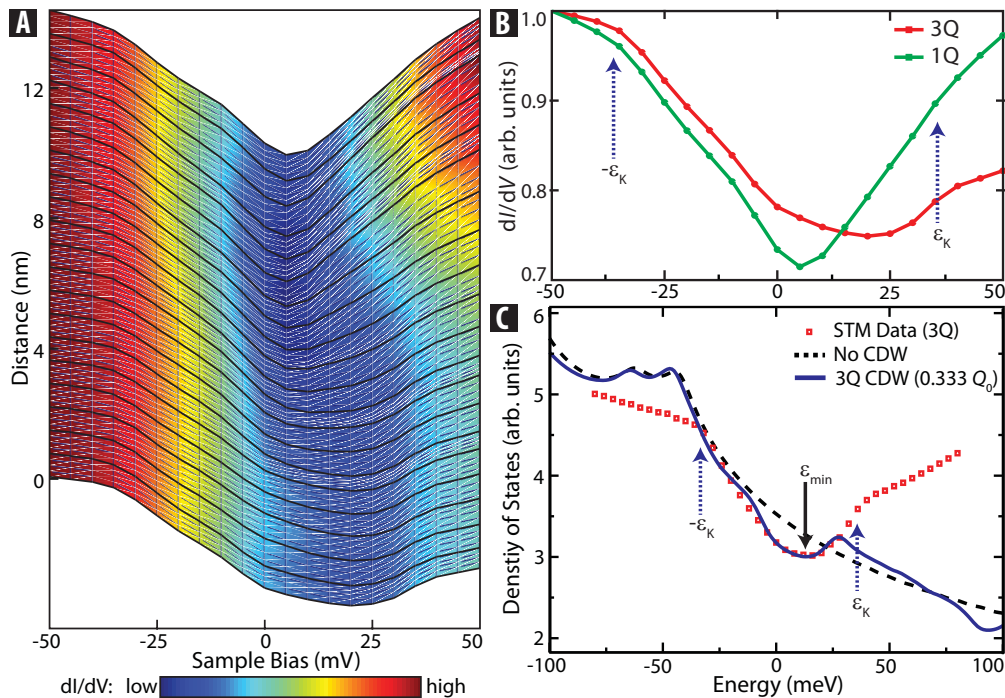


Figure 5: **Spectroscopy across the 1Q – 3Q Interface.** (A) Linecut of dI/dV spectra across the 1Q – 3Q interface taken along the red arrow in Fig. 2A. (B) Representative spectra in the 3Q (red) and 1Q (green) regions of Fig. 2A overlaid for comparison. The 1Q spectra have a minimum close to ϵ_F , a deep V-shape with reduced asymmetry, and kinks at $\pm\epsilon_K$. The spectra are normalized at -50 mV. Setpoint parameters: $V_{\text{sample}} = -50$ mV; $R_J = 0.2$ G Ω ; $V_{\text{mod}} = 3.5$ mV. (C) Calculated DOS for NbSe₂ in the ‘normal’ state (black) and in the presence of a 3Q CDW (blue) using $\tilde{q} = 0.333 Q_0$, $\tilde{\Delta} = 12$ mV, $\tilde{\Gamma} = 5$ mV, compared with the 3Q STM spectrum (red) (details in § SI IV). The calculations reproduce the observed asymmetry, offset ϵ_{min} , and shape of the gap structure.

ful tuning parameter to access the necessary proximate phases for comparison.

Beyond providing new insight into the nature of the 3Q CDW in NbSe₂, our work motivates the utility of the 1Q – 3Q interface in NbSe₂ as a platform to explore competing quantum phases in the weakly correlated limit, as a step towards understanding them in strongly correlated systems. In the Landau picture of CDWs[24], a quantum phase transition between 3Q and 1Q states can arise by tuning the coefficient of the interaction term between the three inequivalent CDW propagation directions (though in our case, the magnitude of q differs between the two states). In NbSe₂, even at low temperatures $T \ll T_{\text{CDW}}$, where the amplitude of the order parameter is already large, moderate strain is seen to have a strong influence, indicating that the system is intrinsically close to the QCP separating these states. We note that a related phase transition between the observed 1Q CDW phase and a ‘hidden’ 2Q phase has been suggested, but not directly visualized, in the rare-earth tellurides[27, 28].

Our discovery provides a new perspective on the role of density wave order in complex systems. First, our res-

olution of two longstanding debates about NbSe₂ puts this much-studied material on firmer footing as a well-understood model system for CDW studies and competing ground states in superconductors. We have disentangled the true CDW gap, and clarified that FS nesting plays a minor role in determining the CDW wavevectors in this material, thereby highlighting the role of other mechanisms in driving the transition. Second, our revelation of a particle-hole asymmetric CDW gap emphasizes the limitations of filled-state-only probes, e.g. ARPES, for investigating phases other than SC - which is unambiguously particle-hole symmetric. Full spectral probes such as STM, in combination with quantitative calculations, are necessary to understand the competition between SC and particle-hole asymmetric phases. Third, our observation of the local effect of even moderate strain in driving a quantum phase transition calls for a reinvestigation of possible phase inhomogeneity in other strongly correlated systems, where larger strain may occur[29, 30].

In the cuprate superconductors, an analogous phase boundary between unidirectional (1Q) charge ‘stripes’ and bidirectional (2Q) ‘checkerboard’ has been

predicted[31, 32]. The introduction of quenched disorder results in discommensurations in the $2Q$ phase and disordered orientational order in the $1Q$ phase, making them hard to distinguish - especially in the cuprate BSCCO, thought to be in proximity to the $1Q - 2Q$ phase boundary[31, 32]. Recent STM studies of the $\sim 4 a_0$ charge order in BSCCO have had conflicting interpretations, with independent suggestions of fluctuating $2Q$ and $1Q$ order[33, 34]. However, the influence of strain, from the supermodulation lattice buckling, or from randomly distributed dopants, is seldom accounted for. Previous studies have shown that both these strain phenomena correlate with nanoscale electronic inhomogeneity[29, 35]. A possible explanation is local stabilization of the $1Q$ state, producing $1Q-2Q$ and $1Q-1Q$ interfaces with spectral differences, analogous to Fig. 2 and Fig. 5A-B. While the presence of strong disorder (up to 12% strain variations on a nanometer length scale[29]) complicates the interpretations in BSCCO, we stress the importance of isolating and modeling strain effects for better understanding and control of the phase transitions in cuprates. Finally, the microscopic visualization of the role of strain in stabilizing new order suggests a controlled route towards engineering novel quantum phases and interfaces and studying symmetry breaking in strongly correlated materials. In this regard, we suggest a connection to the emerging importance of strain as a route to high- T_C superconductivity in novel iron-based materials[36, 37].

D. METHODS

STM Experiments. Measurements were performed using a home-built STM at temperatures between 2 – 10 K. Magnetic fields of up to 5 T were used to suppress the superconducting state as needed. Single crystals of $2H\text{-NbSe}_2$ were cleaved in situ in cryogenic ultrahigh-vacuum and inserted into the STM. A mechanically cut PtIr tip, cleaned by field emission and characterized on gold, was used for the measurements. Spectroscopy data were acquired using a lock-in technique at 1.115 kHz. The topographic and spectroscopic signatures of the $1Q$ ribbons have been verified with several tips.

Band Structure and DOS Calculations. The band structure of $2H\text{-NbSe}_2$ close to ε_F consists of two Nb- $4d$ derived bands and one Se- $4p$ ‘pancake’-shaped hole pocket[6]. The Nb- $4d$ bands are modeled using a tight-binding fit to the observed ARPES band structure[15], and the Se- $4p$ pocket is approximated by a simple

quadratic form to fit LDA calculations[6] (details in § SI III). Using all three bands, the DOS in the presence of a CDW is calculated by imposing a constant coupling between electronic states connected by any one of the three q -vectors. The strength of the coupling $\tilde{\Delta}$ is taken as a free parameter in the reproduction of the experimentally observed DOS, and the size of \tilde{q} is allowed to vary slightly around the observed value of $0.328 Q_0$ (details in § SI IV).

Acknowledgements. We are grateful to Patrick Lee and Steve Kivelson for insightful discussions and to Wilfried Krüger, Lutz Kipp and Daniel Walkup for useful experimental inputs. This work was supported by NSF DMR-0847433 and the New York Community Trust - George Merck Fund (Harvard), DOE, Office of Science, under Contract No. DE-AC02-06CH11357 (Argonne) and DFG via SFB 855 (Kiel). In addition, we acknowledge funding from A*STAR, Singapore (A.S.) and NSERC, Canada (M.M.Y.).

Author Contributions. A.S., M.M.Y. and Y.H. performed STM experiments, and A.S. led the data analysis with contributions from M.M.Y. D.J.R. and K.R. grew and characterized samples. J.v.W., K.R. and M.R.N. performed calculations. A.S. wrote the main manuscript with theoretical sections written by J.v.W. E.W.H., K.R., M.R.N. and J.E.H. advised the work and edited the manuscript.

Author Information. The authors declare no competing financial interests. Correspondence and requests for materials should be addressed to A.S. (anjan@physics.harvard.edu) and J.E.H. (jhoffman@physics.harvard.edu).

* Electronic address: anjan@physics.harvard.edu

† Electronic address: jhoffman@physics.harvard.edu

- [1] S. Sachdev, *Science* **288**, 475 (2000).
- [2] M. R. Norman, D. Pines, and C. Kallin, *Advances in Physics* **54**, 715 (2005).
- [3] D. C. Johnston, *Advances in Physics* **59**, 803 (2010).
- [4] D. Jérôme and H. J. Schulz, *Advances in Physics* **51**, 293 (2002).
- [5] S. A. Kivelson, I. P. Bindloss, V. Oganeyan, J. M. Tranquada, A. Kapitulnik, and C. Howald, *Reviews of Modern Physics* **75**, 1201 (2003).
- [6] M. D. Johannes, I. I. Mazin, and C. A. Howells, *Physical Review B* **73**, 205102 (2006).
- [7] H. Suderow, V. G. Tissen, J. P. Brison, J. L. Martínez, and S. Vieira, *Physical Review Letters* **95**, 117006 (2005).

- [8] T. Kiss, T. Yokoya, A. Chainani, S. Shin, T. Hanaguri, M. Nohara, and H. Takagi, *Nature Physics* **3**, 720 (2007).
- [9] Y. Feng, J. Wang, R. Jaramillo, J. van Wezel, S. Haravifard, G. Srajer, Y. Liu, Z. A. Xu, P. B. Littlewood, and T. F. Rosenbaum, *Proceedings of the National Academy of Sciences* **109**, 7224 (2012).
- [10] D. E. Moncton, J. D. Axe, and F. J. DiSalvo, *Physical Review Letters* **34**, 734 (1975).
- [11] J. A. Wilson, F. J. D. Salvo, and S. Mahajan, *Advances in Physics* **50**, 1171 (2001).
- [12] S. V. Borisenko, A. A. Kordyuk, V. B. Zabolotnyy, D. S. Inosov, D. V. Evtushinsky, B. Büchner, A. N. Yaresko, A. Varykhalov, R. Follath, W. Eberhardt, et al., *Physical Review Letters* **102**, 166402 (2009).
- [13] A. Mialitsin, Phd, Rutgers University (2010).
- [14] F. Weber, S. Rosenkranz, J.-P. Castellan, R. Osborn, R. Hott, R. Heid, K.-P. Bohnen, T. Egami, A. Said, and D. Reznik, *Physical Review Letters* **107**, 107403 (2011).
- [15] D. J. Rahn, S. Hellmann, M. Kalläne, C. Sohrt, T. K. Kim, L. Kipp, and K. Rossnagel, *Physical Review B* **85**, 224532 (2012).
- [16] T. Straub, T. Finteis, R. Claessen, P. Steiner, S. Hüfner, P. Blaha, C. S. Oglesby, and E. Bucher, *Physical Review Letters* **82**, 4504 (1999).
- [17] K. Rossnagel, O. Seifarth, L. Kipp, M. Skibowski, D. Voß, P. Krüger, A. Mazur, and J. Pollmann, *Physical Review B* **64**, 235119 (2001).
- [18] T. Valla, A. V. Fedorov, P. D. Johnson, P.-A. Glans, C. McGuinness, K. Smith, E. Y. Andrei, and H. Berger, *Physical Review Letters* **92**, 086401 (2004).
- [19] D. W. Shen, Y. Zhang, L. X. Yang, J. Wei, H. W. Ou, J. K. Dong, B. P. Xie, C. He, J. F. Zhao, B. Zhou, et al., *Physical Review Letters* **101**, 226406 (2008).
- [20] H. F. Hess, R. B. Robinson, and J. V. Waszczak, *Physica B: Condensed Matter* **169**, 422 (1991).
- [21] W. L. McMillan, *Physical Review B* **14**, 1496 (1976).
- [22] H. Wang, J. Lee, M. Dreyer, and B. I. Barker, *Journal of Physics: Condensed Matter* **21**, 265005 (2009), ISSN 0953-8984.
- [23] H. Bando, Y. Miyahara, H. Enomoto, and H. Ozaki, *Surface Science* **381**, L609 (1997).
- [24] W. L. McMillan, *Physical Review B* **12**, 1187 (1975).
- [25] M. R. Norman, A. Kanigel, M. Randeria, U. Chatterjee, and J. C. Campuzano, *Physical Review B* **76**, 174501 (2007).
- [26] J. R. Kirtley, S. Washburn, and D. J. Scalapino, *Physical Review B* **45**, 336 (1992).
- [27] H. Yao, J. A. Robertson, E.-A. Kim, and S. A. Kivelson, *Physical Review B* **74**, 245126 (2006).
- [28] N. Ru, C. L. Condon, G. Y. Margulis, K. Y. Shin, J. Laverock, S. B. Dugdale, M. F. Toney, and I. R. Fisher, *Physical Review B* **77**, 035114 (2008).
- [29] J. A. Slezak, J. Lee, M. Wang, K. McElroy, K. Fujita, B. M. Andersen, P. J. Hirschfeld, H. Eisaki, S. Uchida, and J. C. Davis, *Proceedings of the National Academy of Sciences* **105**, 3203 (2008).
- [30] J.-H. Chu, J. G. Analytis, K. De Greve, P. L. McMahon, Z. Islam, Y. Yamamoto, and I. R. Fisher, *Science* **329**, 824 (2010).
- [31] J. A. Robertson, S. A. Kivelson, E. Fradkin, A. C. Fang, and A. Kapitulnik, *Physical Review B* **74**, 134507 (2006).
- [32] A. Del Maestro, B. Rosenow, and S. Sachdev, *Physical Review B* **74**, 024520 (2006).
- [33] W. D. Wise, M. C. Boyer, K. Chatterjee, T. Kondo, T. Takeuchi, H. Ikuta, Y. Wang, and E. W. Hudson, *Nature Physics* **4**, 696 (2008).
- [34] C. V. Parker, P. Aynajian, E. H. da Silva Neto, A. Pushp, S. Ono, J. Wen, Z. Xu, G. Gu, and A. Yazdani, *Nature* **468**, 677 (2010).
- [35] I. Zeljkovic, Z. Xu, J. Wen, G. Gu, R. S. Markiewicz, and J. E. Hoffman, *Science* **337**, 320 (2012).
- [36] S. R. Saha, N. P. Butch, T. Drye, J. Magill, S. Ziemak, K. Kirshenbaum, P. Y. Zavalij, J. W. Lynn, and J. Paglione, *Physical Review B* **85**, 024525 (2012), ISSN 1098-0121.
- [37] Q.-Y. Wang, Z. Li, W.-H. Zhang, Z.-C. Zhang, J.-S. Zhang, W. Li, H. Ding, Y.-B. Ou, P. Deng, K. Chang, et al., *Chinese Physics Letters* **29**, 037402 (2012).
- [38] T. Hanaguri, K. Igarashi, M. Kawamura, H. Takagi, and T. Sasagawa, *Physical Review B* **82**, 1 (2010).
- [39] G. M. Rutter, J. N. Crain, N. P. Guisinger, T. Li, P. N. First, and J. A. Stroscio, *Science* **317**, 219 (2007).
- [40] Y. Okada, W. Zhou, D. Walkup, C. Dhital, S. D. Wilson, and V. Madhavan, *Nature Communications* **3**, 1158 (2012).
- [41] M. J. Lawler, K. Fujita, J. Lee, A. R. Schmidt, Y. Kohsaka, C. K. Kim, H. Eisaki, S. Uchida, J. C. Davis, J. P. Sethna, et al., *Nature* **466**, 347 (2010).
- [42] M. H. Hamidian, I. A. Firmo, K. Fujita, S. Mukhopadhyay, J. W. Orenstein, H. Eisaki, S. Uchida, M. J. Lawler, E.-A. Kim, and J. C. Davis, *New Journal of Physics* **14**, 053017 (2012).
- [43] T. L. Williams, Phd, Harvard University (2011).
- [44] J. R. Kirtley and D. J. Scalapino, *Physical Review Letters* **65**, 798 (1990).
- [45] F. C. Niestemski, S. Kunwar, S. Zhou, S. Li, H. Ding, Z. Wang, P. Dai, and V. Madhavan, *Nature* **450**, 1058 (2007), ISSN 1476-4687.
- [46] I. Fridman, K.-W. Yeh, M.-K. Wu, and J. Y. T. Wei, *Journal of Physics and Chemistry of Solids* **72**, 483 (2011).
- [47] T. Arai, K. Ichimura, K. Nomura, S. Takasaki, J. Yamada, S. Nakatsuji, and H. Anzai, *Physical Review B* **63**, 104518 (2001).
- [48] K. Rahnejat, C. Howard, N. Shuttleworth, S. Schofield, K. Iwaya, C. Hirjibehedin, C. Renner, G. Aeppli, and M. Ellerby, *Nature Communications* **2**, 558 (2011).
- [49] R. T. Collins, J. Lambe, T. C. McGill, and R. D. Burnham, *Applied Physics Letters* **44**, 532 (1984).
- [50] W. McMillan and J. Mochel, *Physical Review Letters* **46**, 556 (1981).

SUPPORTING INFORMATION

SI I. SAMPLE CHARACTERIZATION

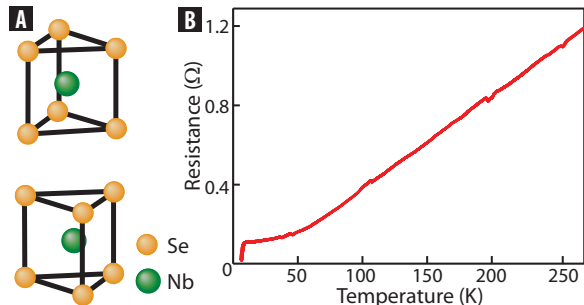


Figure S1: **Sample Characterization.** (A) The layered hexagonal crystal structure of $2H\text{-NbSe}_2$, with alternating sandwiches of Se-Nb-Se. (B) Temperature dependence of the resistance for the sample batch used for this study, showing a superconducting transition at ~ 7 K.

$2H\text{-NbSe}_2$ is a layered transition metal dichalcogenide with a hexagonal structure and D_{6h}^4 space group symmetry. The unit cell (Fig. S1A) consists of two sandwiches of Se-Nb-Se. The crystal typically cleaves between the neighboring Se layers, coupled by weak van der Waals forces.

Single crystals of $2H\text{-NbSe}_2$ were grown by chemical vapor transport using iodine as the transport agent. A transport characterization of the sample batch used in this work is shown in Fig. S1B. The superconducting transition is observed at $T_{SC} \sim 7$ K. The residual resistivity ratio (RRR), defined as the ratio of resistances $R(295\text{ K})/R(7.5\text{ K})$, is ~ 16 .

SI II. 1Q 'RIBBONS': HEIGHT AND ORIENTATION

The 1Q CDW typically appears in regions which persist in one direction with apparent 20 – 40 pm topographic elevation, forming a 10 – 20 nm wide 'ribbon' structure (Fig. S2A-C). We note that the topographic elevation $z_{STM}(\vec{r}, V_0, I_0)$ as measured by maintaining a constant current I_0 with bias setpoint V_0 at lateral tip position $\vec{r} \equiv (x, y)$ can be given by

$$z_{STM}(\vec{r}, V_0, I_0) \simeq z_T(\vec{r}) + \frac{1}{\kappa(\vec{r})} \cdot \ln \left(\frac{I_0}{\int_0^{V_0} dV eD(\vec{r}, eV)} \right) \quad (S1)$$

Here $z_T(\vec{r})$ is the true topographic corrugation of the sample, $\kappa(\vec{r})$ is a measure of the local tunnel barrier height (LBH), and $D(\vec{r}, eV)$ is the local density of states (LDOS) of the sample at energy eV . Because of the logarithmic sensitivity of $z_{STM}(\vec{r}, V_0, I_0)$ to the integral of the LDOS from the Fermi energy, ε_F (corresponding to $V = 0$) up to the bias setpoint eV_0 , STM topographs may contain electronic artifacts masquerading as geometric effects. Therefore, we present two pieces of evidence for the true geometric elevation of these ribbons.

First, a tabulation of the relative orientation θ_{R, Q_0} of the ribbon to the nearest Bragg vector of the underlying hexagonal lattice for the various ribbons imaged in the study shows a seemingly random spread from -30° to 30° - the full range of available angles (Fig. S2D-E). Furthermore, these ribbon structures can intersect to form X as well as Y junctions (Fig. S2A-B), and the angle between intersecting ribbons varies from 40° to 60° . The fact that ribbon orientation does not respect lattice symmetry strongly suggests a true geometric, rather than electronic origin of their apparent height. We contrast this observation with enhanced STM topographic corrugation associated with predominantly electronic features in a wide range of other materials, which respect the symmetry of the hexagonal[38, 39] or square[33] lattice.

Second, the measured height of these ribbons in STM topographs exhibits $< 5\%$ dependence on bias setpoint within 400 mV below the Fermi energy (Fig. S3A-C). We note that this energy range over which the measured height of the ribbons is invariant is much larger than the spectral range of CDW variation in the DOS (~ 50 mV). We further note the contrast between the bias-independent ribbons, and single atom impurity resonances, whose measured 'height' varies by 50 – 70% between Fig. S3A and B. Therefore we conclude that the measured height (20 – 40 pm) and width (10 – 20 nm) of these ribbons has a predominantly geometric origin.

Having established the topographic origin of these ribbons (Fig. S2 and Fig. S3), we suggest that these ribbons are likely a topographic rippling of the top few lay-

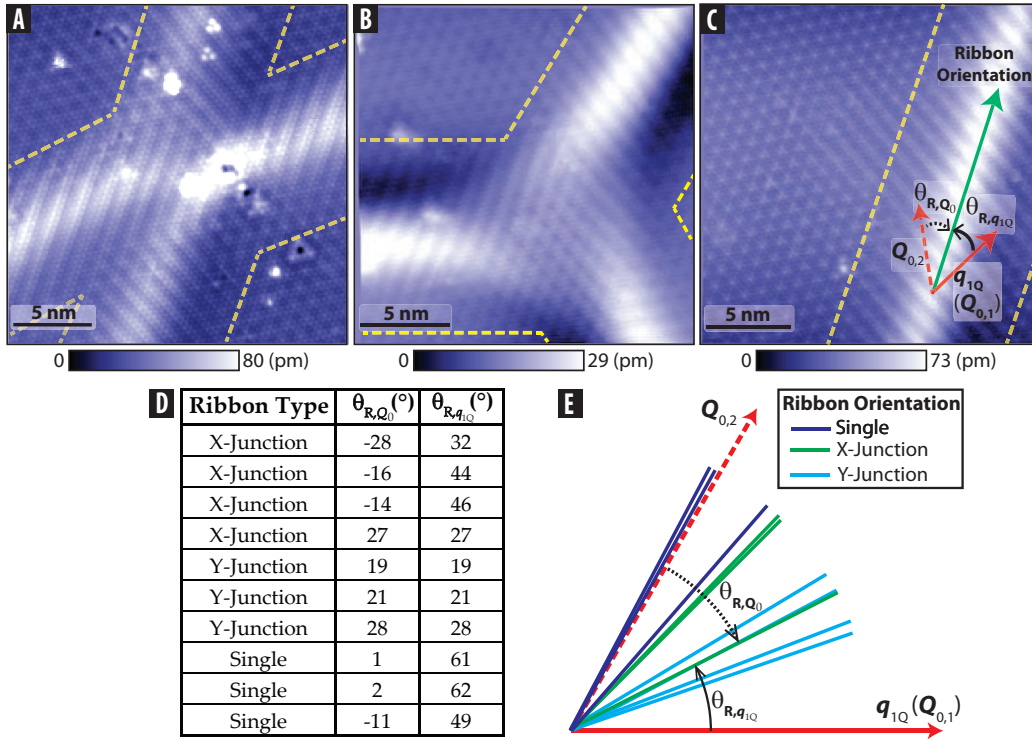


Figure S2: **1Q 'Ribbons': Orientation.** (A, B) STM topographs showing 'ribbons' of unidirectional (1Q) CDW, intersecting to form an X-junction (A) and a Y-junction (B), with CDW wavevector \vec{q}_{1Q} varying between the arms. Dashed yellow lines indicate the approximate extent of the ribbons. Setpoint parameters: $V_{\text{sample}} = -50$ mV for both; $R_J = 5$ G Ω (A), 1 G Ω (B). (C) STM topograph of a 1Q - 3Q interface (top arm of X-junction, also shown in Fig. 2B), demonstrating the definitions of the relative orientations θ_{R,Q_0} , between the ribbon (green arrow) and the nearest Bragg vector (dashed red arrow), and $\theta_{R,q_{1Q}}$, between the ribbon and 1Q wavevector \vec{q}_{1Q} (solid red arrow). (D) A table detailing the values of θ_{R,Q_0} and $\theta_{R,q_{1Q}}$ observed in the various 1Q ribbons studied in this work, with the first entry corresponding to C. (E) A visual illustration of the spread of values in table D. The dark blue (single), green (X-junction) and cyan (Y-junction) lines describe the orientation of the various ribbons with respect to the 1Q wavevector \vec{q}_{1Q} along the $\vec{Q}_{0,1}$ Bragg vector (solid red arrow) and another Bragg vector $\vec{Q}_{0,2}$ (dashed red arrow).

ers. These ribbons may arise during the cleaving process due to underlying growth defects which can intercalate between Se-Nb-Se sandwich layers. We note that similar topographic ribbon deformations have recently been observed in another layered chalcogenide (Bi₂Te₃)[40].

We estimate the in-plane and out-of-plane lattice strain associated with the topographic ribbon features. Using the maximum topographic elevation of an observed ribbon (40 pm), we can put an upper limit on the out-of-plane distortion by assuming that a minimum of 2 sandwich layers are elevated (any fewer, and the defects causing the elevation would be likely visible in our topographs). The out of plane distortion is therefore $\lesssim 3\%$ (40 pm/12.54 Å) of the unit cell spacing. To measure the in-plane distortion, we first use the Lawler-Fujita algorithm[41], which can determine the lateral location of atoms with precision $\sim 2\%$ of the lattice spacing[42, 43]. With this algorithm, we do not observe any change in the lattice constant across the rib-

bon, which places a direct experimental upper limit on the in-plane distortion of $\sim 2\%$.

However, we can estimate the actual in-plane distortion indirectly from the measured out-of-plane distortion, by modeling the ribbon as a half-period of a sinusoid with height h (40 pm) and width W (10 nm) (Fig. S3D). The total lateral deformation due to such a ribbon is $\delta W \sim 45$ pm, corresponding to $\sim 0.06\%$ of the lattice spacing. As this is well below the resolution of the Lawler-Fujita algorithm, it is not surprising that the in-plane distortion is not detectable in STM topographs. From the upper bounds of 3% on the vertical strain and 0.06% on the lateral strain, we note that the magnitude of the strain field leading to the formation of these ribbons is moderate, in comparison to some other correlated materials[29, 30]. We also note that while the magnitude of lattice distortion of these ribbons may seem small in the context of the observed quantum phase inhomogeneity, a comparison with other known materials

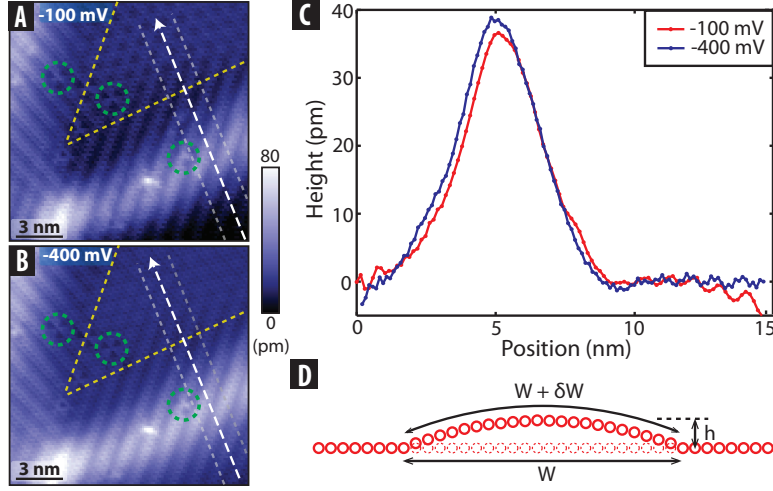


Figure S3: 1Q ‘Ribbons’: Bias Setpoint Dependence. (A, B) Topographs of 1Q ribbons over the same spatial area acquired with different bias setpoints: -100 mV (A) and -400 mV (B), with $R_J = 10 \text{ G}\Omega$ in both. The dashed yellow lines indicate the approximate extent of the ribbons, and the dashed green circles enclose triangular impurities, visible in B with a 50 – 70% larger apparent height than in A. (C) Linecuts taken through the topographs in A (red) and B (blue) transverse to the lower ribbon, along the dashed white arrows. The measured ribbon height varies less than 5% between bias setpoints -100 mV and -400 mV. The linecuts have been laterally averaged over a 3 nm width indicated by the dashed grey lines. (D) A cartoon representation of the lattice distortion caused by the formation of such a ribbon, modeled as a half period of a sinusoid. The red circles correspond to rows of displaced Se atoms, while the dashed red circles represent their original undistorted positions. The ribbon has height h (40 pm) and width W (10 nm), resulting in a total lateral distortion of $\delta W \sim 45 \text{ pm}$ across the ribbon.

suggests that strain of this magnitude can be sufficient to drive a transition to the unidirectional CDW phase[28].

We previously discussed the ribbon orientation with respect to the lattice (θ_{R,Q_0}); we now consider the ribbon orientation with respect to the 1Q CDW wavevector ($\theta_{R,q_{1Q}}$), also detailed in Fig. S2D-E. In a simple picture of the strained ribbon structure, we would expect the ribbon-induced strain to couple strongly to the 1Q CDW orientation either parallel or perpendicular to the ribbon, and thus we would expect to observe values of $\theta_{R,q_{1Q}}$ either between $0 - 30^\circ$ or between $60 - 90^\circ$. Yet we often find $\theta_{R,q_{1Q}}$ to be in the $30 - 60^\circ$ range as well. Insufficient statistics prevent us from inferring a clear connection between ribbon orientation and \vec{q}_{1Q} orientation, but the wide distribution of relative angles suggests the complexity of the interaction.

SI III. BAND STRUCTURE CALCULATIONS

The band structure of $2H\text{-NbSe}_2$ close to ε_F consists of two Nb-4d derived bands and one Se-4p ‘pancake’-shaped hole pocket[6, 17]. Close to ε_F , the Se-4p pancake-shaped hole pocket which surrounds the Γ -point can be modeled by a simple quadratic form,

$$E = A \cdot \frac{a_0^2}{4\pi^2} (k_x^2 + k_y^2) + B \quad (\text{S2})$$

With the values of $A = -5.4 \text{ eV}$ and $B = -0.65 \text{ eV}$, this model accurately reproduces the dispersion obtained in LDA calculations by Johannes *et al.*[6], as shown in Fig. S4A. To model the Nb-4d bands, we use a tight-binding fit to the band structure observed in ARPES experiments, as reported by Rahn *et al.*[15]. We find that a small ($\sim +16 \text{ meV}$) offset in the chemical potential relative to the parameters used by Rahn *et al.* was needed to reproduce the observed DOS from STM measurements. This offset is within the accuracy of the tight-binding fitting scheme[15]. The band energies of the tight-binding description are given by[15]

$$\begin{aligned} E = & t_0 + t_1[2 \cos \xi \cos \eta + \cos 2\xi] \\ & + t_2[2 \cos 3\xi \cos \eta + \cos 2\eta] \\ & + t_3[2 \cos 2\xi \cos 2\eta + \cos 4\xi] \\ & + t_4[\cos \xi \cos 3\eta + \cos 5\xi \cos \eta + \cos 4\xi \cos 2\eta] \\ & + t_5[2 \cos 3\xi \cos 3\eta + \cos 6\xi] \end{aligned} \quad (\text{S3})$$

where $\xi = \frac{1}{2}k_x a_0$ and $\eta = \frac{1}{2}\sqrt{3}k_y a_0$ and k_y is along

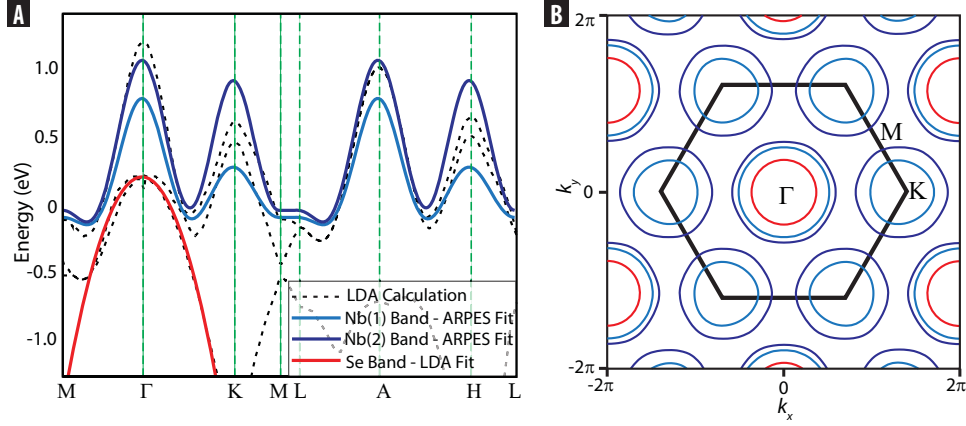


Figure S4: **Band Structure Calculations.** (A) The calculated band structure of $2H\text{-NbSe}_2$ along high-symmetry directions, showing the two Nb- $4d$ bands obtained using an ARPES tight-binding fit[15], and the Se- $4p$ band, modeled as a parabolic fit to LDA calculations of Johannes *et al.*[6], compared with the LDA calculations (dashed black lines). (B) The Fermi surface obtained using this band structure fit, with the BZ shown in black.

$\Gamma - M$. The values of the tight binding parameters (including the offset) used in this work are:

Parameter	Nb Band (1)	Nb Band (2)
t_0	26.9	219.0
t_1	86.8	46.0
t_2	139.9	257.5
t_3	29.6	4.4
t_4	3.5	-15.0
t_5	3.3	6.0

Table S1: Tight-binding parameters for the two Nb bands (in meV).

SI IV. DENSITY OF STATES CALCULATIONS

To calculate the DOS in the presence of a $3Q$ CDW, we impose a coupling between states connected by any one of the three \vec{q} -vectors, given by:

$$\mathcal{H}_{\text{CDW}} = \tilde{\Delta} \cdot \sum_{\vec{k}} \left(c_{\vec{k}+\vec{q}}^\dagger c_{\vec{k}} + \text{h.c.} \right) \quad (\text{S4})$$

The strength $\tilde{\Delta}$ of the coupling is taken as a free parameter in the reproduction of the experimentally observed DOS, with a broadening parameter fixed at $\Gamma = 5$ meV. Adjusting the size of \vec{q} slightly around the observed value of $q_{3Q} = 0.328 Q_0$, we find the best match with STM spectra using $\vec{q} = 0.333 Q_0$ (corresponding to the locally commensurate CDW periodicity), $\tilde{\Delta} = 12$ meV.

With these parameter values, the gap structure in the calculated DOS closely approaches the overall shape, width and center of the gap structure seen in the measured data within ± 30 meV of the Fermi energy ε_F , as shown in Fig. 5C.

To demonstrate the accuracy of this fit, we show the effects of varying the wavevector \vec{q} by 1 – 2% (Fig. S5A-B), and the gap value $\tilde{\Delta}$ by 10 – 20% (Fig. S5C-D). Using these fit parameter variations, we estimate the errors for \vec{q} and $\tilde{\Delta}$ to be $0.004 Q_0$ and 2 meV respectively. The value of $\tilde{\Delta}$ may however be an overestimate, leading to a systematic error of the same order as the fit uncertainty, since the described procedure does not take into account the particle-hole symmetric inelastic background in the experimental DOS. Accurate modeling of the inelastic background would require detailed temperature dependent spectroscopic data, which is beyond the scope of this work.

Crucially, we note that the particle-hole asymmetry in the CDW gap, with its minimum centered above ε_F , cannot be removed by the subtraction of a particle-hole symmetric background. Likewise, the striking deviation of our fitted gap parameter ($\tilde{\Delta} = 12$ meV) from previous results (four times larger than the 3 meV value detailed by Borisenko *et al.*[12], and three times smaller than the 35 meV value detailed by Hess *et al.*[20]) far exceeds fit or systematic uncertainties.

To experimentally verify the lack of bearing of the 35 mV kinks on the CDW phase, we performed spectroscopy up to 45 K, and universally observed the presence of these kinks in the STM spectra well above T_{CDW} (~ 33 K). A comparison of the typical spectrum ac-

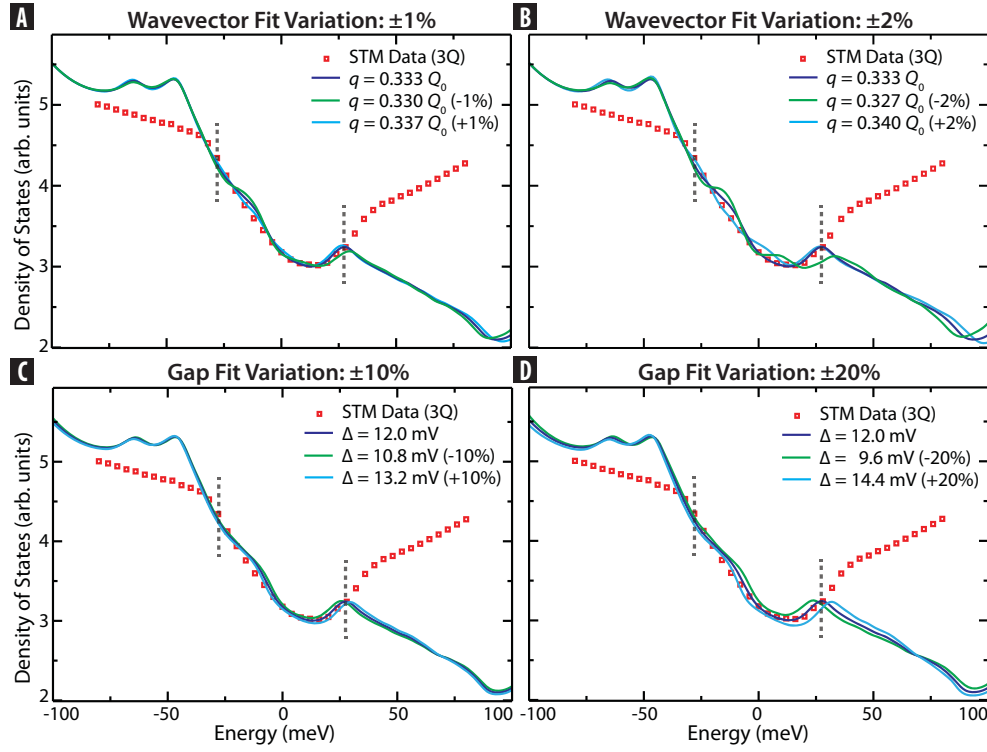


Figure S5: **Variations in DOS Fit Parameters.** Calculated DOS spectrum using the band structure fit in the presence of a 3Q CDW, showing the effects of varying the fit parameters, wavevector \tilde{q} and gap value $\tilde{\Delta}$ around the best fit values ($\tilde{q} = 0.333 Q_0$, $\tilde{\Delta} = 12$ meV, dark blue), compared with the STM data (red). (A, B) show the effects of varying the wavevector \tilde{q} around $0.333 Q_0$ by $\pm 1\%$ and $\pm 2\%$ respectively. (C, D) show the effects of varying the gap value $\tilde{\Delta}$ around 12 meV by $\pm 10\%$ and $\pm 20\%$ respectively. Error bars for \tilde{q} ($0.004 Q_0$) and $\tilde{\Delta}$ (2 meV) are deduced using these variations.

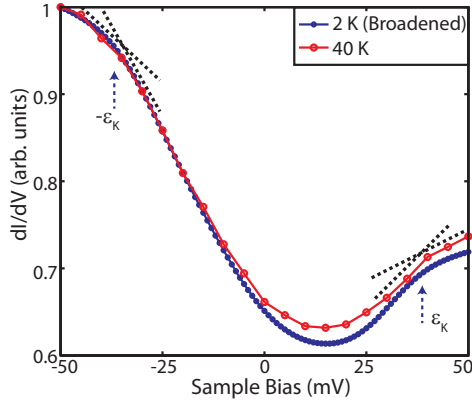


Figure S6: **Spectroscopy above T_{CDW} .** Spectrum acquired at 40 K (red) compared with that acquired at 2 K, 6 T (blue) on the same cleaved surface (within 300 nm). The 2 K spectrum has been thermally broadened to 40 K for ease of comparison. The spectral kinks at ± 35 mV ($\pm \epsilon_K$) are distinguishable well above T_{CDW} , as shown by the guides to the eye (c.f. Fig. 1C for a low temperature comparison).

quired at 40 K to that acquired at 2 K, is shown in Fig. S6. We note that the data acquired at 40 K are thermally

smeared by $\mathcal{O}(3k_B T)$, i.e. ~ 10 mV, resulting in a broadening of the kinks. Despite this, the kinks remain distinguishable, and are present throughout all spatial regions studied in this work.

For completeness, we show in Fig. S7A the calculated DOS in the presence of a 1Q CDW at the experimentally observed wave vector, $q_{1Q} = 0.286 Q_0$, using $\tilde{\Delta} = 12$ meV. The lack of correspondence between this calculation (green curve in Fig. S7A) and the measured dI/dV spectrum (green curve in Fig. 5B) can be attributed to the increased intensity of the inelastic background in the buckled region of the 1Q ribbons. This background is evident in the V-shape of the dI/dV spectrum in Fig. 5B, centered close to ϵ_F , as explained theoretically[26] and observed experimentally across a wide variety of materials[26, 44–50].

We also compare our results to a calculation of the DOS based on a tight-binding fit to the full three-dimensional LDA band structure reported by Johannes *et al.*[6]. The DOS obtained using this 3D LDA fit is compared to the results based on the 2D fit in Fig. S7B. We find that the STM data are best reproduced using

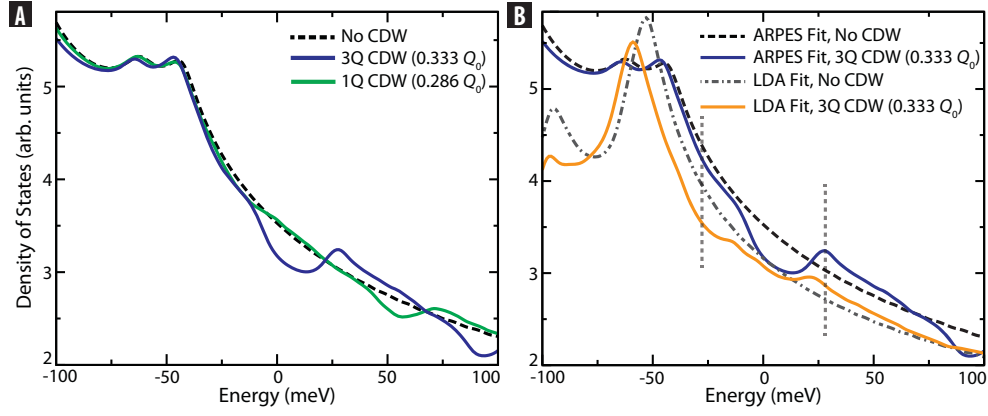


Figure S7: **Comparisons of DOS Calculations.** (A) Calculated DOS spectrum using the ARPES tight-binding fit - in the presence of a 3Q CDW ($\tilde{q} = 0.333 Q_0$, blue) and a 1Q CDW ($q_{1Q} = 0.286 Q_0$, green), with $\tilde{\Delta} = 12$ meV. (B) Calculated DOS spectrum using the tight-binding fit to ARPES data[15] compared with a tight-binding fit to LDA calculations[6] in the 'normal' state and in the presence of a 3Q CDW ($\tilde{q} = 0.333 Q_0$, $\tilde{\Delta} = 12$ meV). The DOS spectrum calculated using the fit to the ARPES data better reproduces the gap feature observed in the STM dI/dV spectrum in Fig. 5C.

the band structure observed by ARPES, and that there is a noticeable difference between the depths of the gaps in the two-dimensional ARPES based and three-dimensional LDA-based band structure fits (despite in-

dependent parameter optimization), which is indicative of some difference between the surface and bulk dispersions[6].